# Langmuir

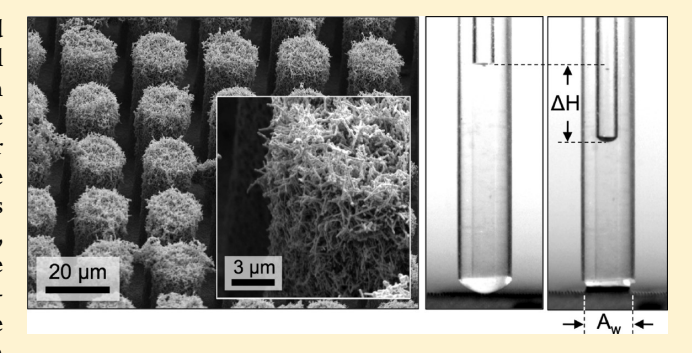
# Role of Wickability on the Critical Heat Flux of Structured Superhydrophilic Surfaces

Md Mahamudur Rahman, Emre Ölçeroğlu, and Matthew McCarthy\*

Department of Mechanical Engineering and Mechanics, Drexel University, 3141 Chestnut Street, Philadelphia, Pennsylvania 19104, United States

Supporting Information

ABSTRACT: While superhydrophilic coatings with enhanced wetting properties have been shown to increase the pool boiling critical heat flux (CHF), the role of nanostructures on its enhancement is not clear. Here, biological templates have been used to demonstrate that wickability is the single factor dictating CHF on structured superhydrophilic surfaces. The flexibility of biotemplating using the Tobacco mosaic virus has been leveraged to create surfaces with varying scales, morphologies, and roughness factors. Their wickabilities have been quantified via the wicked volume flux, a phenomenological parameter analogous to the contact angle, and the role of wickability on CHF has been demonstrated using data from



over three dozen individual surfaces. These results are repeatable and independent of the substrate material, surface fouling, structure material, morphology, and contact angle as well as the structure scale. An experimentally validated correlation for CHF has been reported on the basis of the dimensionless wickability. Additionally, the surfaces have achieved a CHF of 257 W/cm<sup>2</sup> for water, representing the highest reported value to date for superhydrophilic surfaces. While the role of wickability on CHF has often been cited anecdotally, this work provides a quantitative measure of the phenomena and provides a framework for designing and optimizing coatings for further enhancement.

# INTRODUCTION

Through its use in a multitude of applications including power generation, chemical processing, water purification, and HVAC, boiling plays a crucial role in the lives of most people. During boiling, heat transfer is driven by the nucleation, growth, and departure of vapor from a heated surface, with large amounts of energy being transported via the latent heat associated with phase change. 1,2 As the heat flux increases, a competition occurs between the vapor generated at the surface and the replenishing liquid until the critical heat flux (CHF) is reached. CHF is the highest stable heat flux before the transition to film boiling occurs. If the heat flux applied to a surface exceeds the CHF, then a drastic and uncontrollable increase in surface temperature is observed because of the rapid development of an insulating vapor layer blanketing the surface. Because of the importance of CHF in the design and operation of boiling systems, extensive research in this area has been conducted over the last 50 years. While the exact physical mechanisms of CHF are still not fully understood, a variety of correlations and models have been developed showing reasonable agreement with experimental measurements.<sup>3</sup> These models have been based on the stability of liquid-vapor interfaces at high vapor velocities,<sup>4–7</sup> the merging of vapor columns,<sup>8</sup> and macrolayer dry out<sup>9–11</sup> and macrolayer lift off.<sup>12</sup> One of the earliest and most often cited CHF models was proposed by Zuber and focused on the hydrodynamic stability of vapor jets leaving the

heated surface. Additionally, the effects of surface wettability have been studied in several works, 13-15 including Kandlikar's widely cited model based on vapor momentum flux, which incorporates the effects of contact angle and surface orientation. 16 Although deviations from these models are seen, they are still actively cited today because of their general accuracy in predicting CHF on flat surfaces.

The addition of surface structures, however, has been shown to enhance CHF beyond the predictions of these models. 17-33 A variety of publications have reported increased CHF using novel fabrication techniques to create microstructured,  $^{17-20}$ nanostructured, 21-26 and hierarchically structured surfaces 27-30 as well as surfaces with mixed wettability 31,32 and contoured surfaces to control the bubble trajectory. 33 The variability of these designs suggests that CHF enhancement is extremely complex and can be achieved using multiple approaches. One heavily studied method is the use of high-surface-area superhydrophilic coatings with characteristic contact angles approaching 0°. Superhydrophilic surfaces have been demonstrated by numerous researchers including the Cu and Si nanowires fabricated by Chen et al.<sup>21</sup> as well as the hierarchical CuO structures fabricated by Chu et al.<sup>28</sup> These surfaces

Received: August 4, 2014 Revised: August 28, 2014 Published: August 29, 2014

exhibited CHF values for water of up to 200 and 250 W/cm², respectively, as compared to ~75 W/cm² for bare silicon substrates. CHF enhancements have been attributed to a variety of mechanisms, including increased nucleation site densities, <sup>21,22</sup> increased contact line lengths, <sup>18,28</sup> and, most prominently, the ability to transport liquid through the surface structures via capillary wicking. <sup>17,19,21,23,24,26,27,29,30</sup> Capillary wicking provides a means to enhance CHF by maintaining a wetted surface at higher vapor productions and by rewetting dry patches during nucleate boiling. It has been anecdotally cited as a key mechanism by which superhydrophilic surfaces delay the onset of film boiling. However, no quantitative definition of a surface's wickability or a correlation between wickability and CHF enhancement has been clearly demonstrated or accepted to date.

Here, a biotemplated nanofabrication technique based on the self-assembly and metallization of the *Tobacco mosaic virus* (TMV) (Figure 1) has been used to fabricate numerous

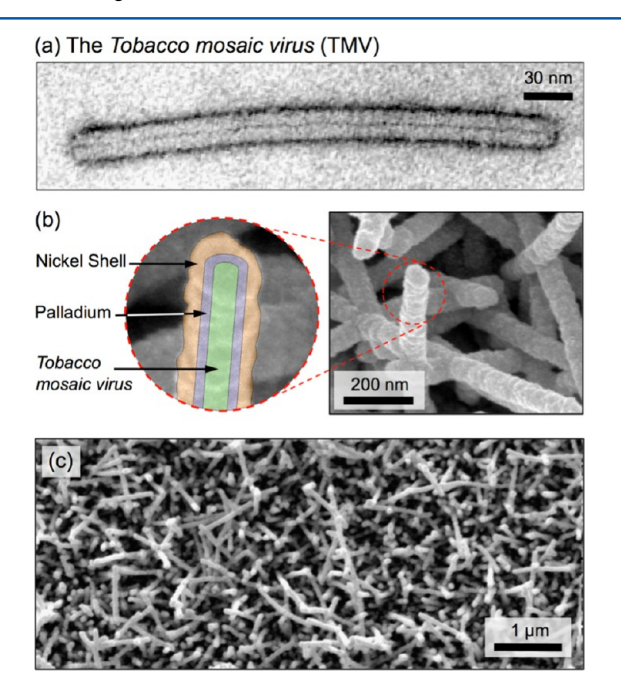


**Figure 1.** Biotemplated nanofabrication. (a) TEM image of the tobacco mosaic virus showing the high-aspect-ratio cylindrical structure. <sup>34</sup> (b) Schematic and SEM image of virus-templated nickel nanostructures. (c) SEM image of surface-bound TMV nanocoatings. (a) Reproduced with permission<sup>34</sup> from the American Chemical Society, 2004.

superhydrophilic surfaces with large variations in the wickability, surface morphology, and roughness factor. The wickability of each surface has been experimentally measured along with its CHF, and a distinct dependency between the two is seen. The results are consistent with predictions using a simple wicking model as well as data from the open literature. This work shows that the wickability of a surface can be quantified and accurately characterized as the maximum wicked volume flux capable of being drawn into the structures and transported past the apparent liquid—vapor—solid contact line on a surface. The experimentally derived correlation relating CHF and wickability shows excellent agreement for over three dozen independent samples fabricated for this work, including those with variations in scale (micro, nano, and hierarchical), substrate material (silicon, aluminum, stainless steel, and

copper), nanostructure density, roughness factor, degradation because of fouling, and structure material and morphology (etched silicon microposts, virus-templated nickel nanostructures, and copper oxide nanostructures).

# ■ BIOTEMPLATED NANOFABRICATION

The TMV is a benign plant virus, and its use as a template for the creation of surface-bound metallic nanostructures on a variety of materials<sup>24,35</sup> and surface morphologies<sup>36–38</sup> has been previously demonstrated for both electrochemical energy storage<sup>36,39</sup> and tailoring wettings properties.<sup>24,37,40</sup> Figure 1a shows a TEM image of the TMV showing its 300-nm-long, 18nm-diameter cylindrical structure.<sup>34</sup> Using a simple solutionbased room-temperature process, core-shell nickel nanostructures can be conformally deposited onto numerous materials without the need for any external power, heat, or special equipment. First, the TMV assembles onto the surface from solution, followed by the successive reduction of palladium and nickel onto the outer surface of the assembled virus. Figure 1b shows an SEM image of the resulting nickel nanostructures and a schematic of the biotemplated core-shell geometry. The TMV acts as a temporary scaffold and plays no part in defining or maintaining the nanostructures after nickel deposition. The coatings are mechanically robust and show no physical degradation or mechanical failure after continuous nucleate boiling, including the repeated occurrence of CHF and burnout,<sup>24</sup> with temperatures exceeding 200 °C. Complete details of the TMV biotemplating process can be found in the Supporting Information.

Biotemplating has been used here to create a multitude of structured surfaces with large variations in the roughness factor and wickability. Figure 2 shows representative SEM images of 8 of the 20 silicon samples fabricated for this work, including 4 microstructured surfaces (Figure 2a-d) as well as 4 hierarchically structured surfaces (Figure 2e-h) composed of nickelcoated TMV conformally assembled onto the corresponding microstructure geometries. Figure 2e-h shows SEM images of the hierarchical surfaces at increasing magnifications, demonstrating the conformal nature of the nickel-coated TMV nanostrutures. The microstructured surfaces were fabricated using deep reactive ion etching of the underlying silicon substrate and are coated with a thin (20-40 nm) layer of nickel to maintain a consistent intrinsic contact angle for all 20 samples. A total of nine different microstructure designs and their corresponding nine hierarchal designs were created, along with two nanostructured samples fabricated on flat silicon substrates. The micropost geometries (diameter × pitch × height) were varied for each design, and combining them with the conformal TMV nanostructures resulted in roughness factors (defined as the actual surface area relative to the footprint area) of r = 1.03-57.24. See the Supporting Information for complete details of the calculation of the roughness factor and its uncertainty. All of the surfaces fabricated in this work demonstrated superhydrophilic behaviors and exhibited no measurable contact angle.

# WICKABILITY AND CHF MODELING

As CHF is approached, the high rate of vapor generation drastically impedes the ability to visualize flow on and near the heated surface. This has been a significant hurdle in understanding the mechanism of CHF, and a likely reason as to why no singularly accepted model exists to predict it.

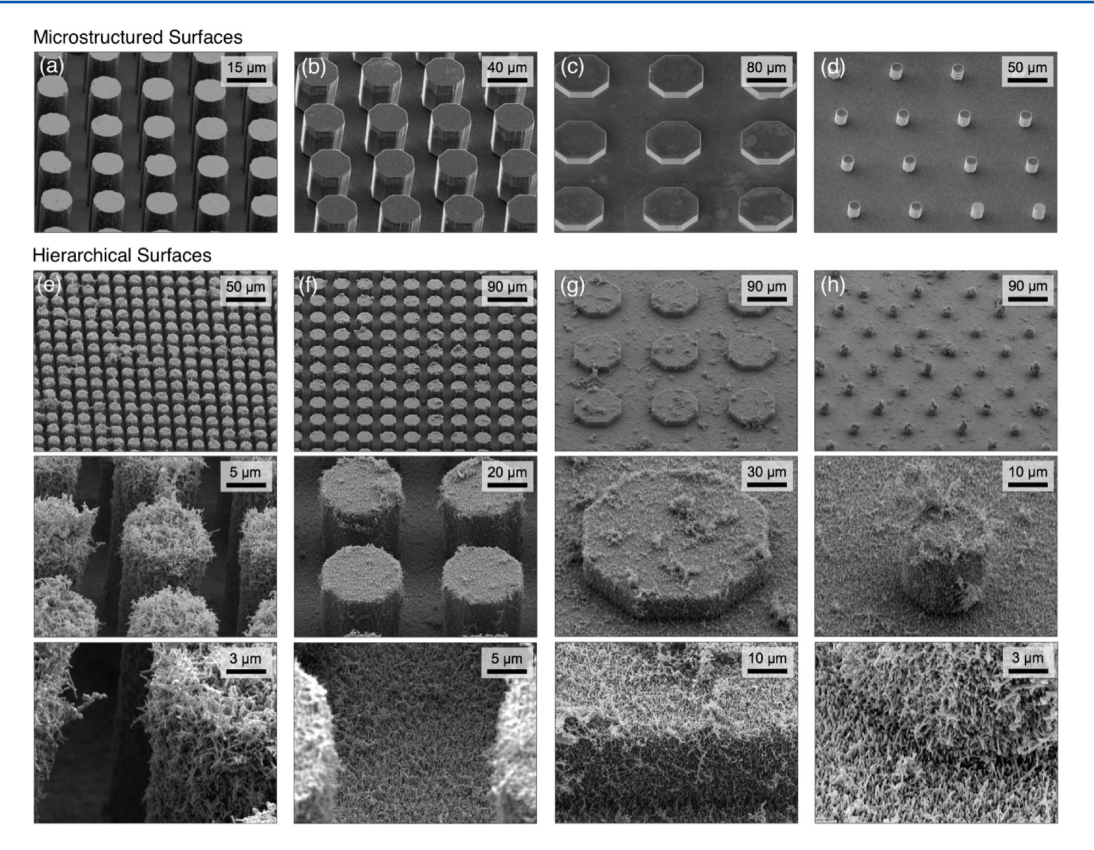


Figure 2. Micro, nano, and hierarchically structured silicon surfaces fabricated to characterize the effect of wickability on pool boiling CHF. (a–d) SEM images of four representative microstructure geometries fabricated using deep reactive ion etching. (e–h) Hierarchical surfaces at three different magnifications composed of the microstructures shown in (a–d) conformally coated with TMV-templated nickel nanostructures. Complete details of the 20 different micro, nano, and hierarchical silicon surfaces characterized in this work are given in Figure Sc, including the microstructure geometry and the resulting roughness factor.

Kutateladze was the first to propose that the hydrodynamic stability was the key to triggering CHF<sup>4,5</sup> and suggested the use of a nondimensional grouping for CHF of

$$K = \frac{q_{\text{CHF}}''}{\rho_{\text{v}}^{1/2} h_{\text{fg}} [\sigma g(\rho_{1} - \rho_{\text{v}})]^{1/4}}$$
(1)

where  $q''_{CHF}$  is the CHF value and  $h_{fe}$ ,  $\sigma$ , g,  $\rho_{v}$ , and  $\rho_{l}$  are the latent heat, surface tension, gravitational acceleration, and vapor and liquid densities, respectively. Using hydrodynamic analysis to determine the critical vapor velocity at CHF, Zuber suggested a value of K = 0.131 based on the Helmholtz instability of vapor columns. Lienhard and Dhir claimed that the critical wavelength of instability should be given by the most dangerous Taylor wavelength, resulting in K = 0.149. Kutateladze, however, found a value of K = 0.16 from the fitting of experimental data.<sup>4,5</sup> In the following decades, many more models have been developed using the nondimensional CHF parameter given by eq 1. Most notably, these include the macrolayer dryout model developed by Haramura and Katto<sup>9</sup> and the associated macrolayer lift-off model developed by Guan et al., 12 which consider vapor stems feeding large mushroom bubbles with a liquid macrolayer underneath (as opposed to the vapor columns suggested by Zuber). These approaches have gained attention in recent years because of their consistency with visual observations and increased accuracy under a wider range of operating conditions. 10,11 For water under atmospheric conditions, the macrolayer dry-out and lift-off models predict values of K = 0.13 and 0.115, respectively.<sup>9,12</sup>

None of these approaches, however, take into account the effects of surface structures, wettability, or wickability and greatly underpredict CHF for superhydrophilic structured surfaces. While Kandlikar's model<sup>16</sup> incorporates the effects of contact angle, the experimental results of CHF consistently exceed its predictions for contact angles approaching zero. This suggests that another mechanism of enhancement is at play in addition to wettability. Chu et al. showed substantial increases in CHF for structured surfaces and presented a model based on Kandlikar's vapor momentum flux incorporating the roughness factor, r, and suggested the increase in the contact line length delays CHF.<sup>18</sup> Guan et al. extended the macrolayer lift-off model to include the effects of capillary wicking through surface structures, where the momentum due to capillary flow acts to hold the liquid macrolayer to the surface, thus delaying CHF.<sup>41</sup> The above discussion of CHF models is by no means an exhaustive review. For a more detailed treatment of the proposed mechanisms triggering CHF and the various predictive models (including the impact of wettability and structures), the authors point to the work of Bergles,<sup>3</sup> Carey,<sup>42</sup> Kandlikar, 16 Lu et al., 23 Kim, 1 and Guan et al. 12

The effect of wickability on CHF can be analyzed through a simple examination of the apparent liquid—vapor—solid contact line on a heated surface. Figure 3 illustrates this, where some fraction of the surface is covered with liquid and another is covered with vapor (i.e., a vapor column, bubble, or stem). While some portion of the liquid is evaporated across the apparent liquid—vapor interface, additional liquid is transported underneath the apparent contact line and evaporated across the

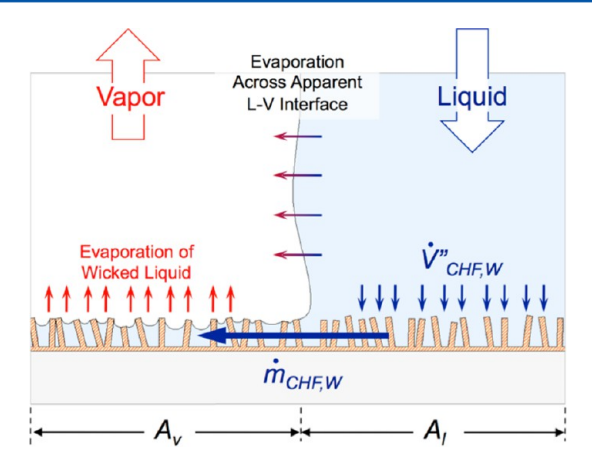


**Figure 3.** Schematic representation of the role of wickability in enhancing the critical heat flux. The wicked liquid is drawn into the nanostructures in the wetted areas, transported underneath the apparent liquid—vapor interface, and evaporated.

complex liquid—vapor interface supported by the surface structures. The increase in CHF for a wicking surface (as compared to the corresponding nonwicking surface) can therefore be related to the latent heat associated with the wicked liquid flow rate and is given by

$$\begin{split} \Delta q_{\text{CHF}}'' &= q_{\text{CHF,W}}'' - q_{\text{CHF,NW}}'' \\ &= \frac{\dot{m}_{\text{CHF,W}} h_{\text{fg}}}{A_{\text{t}}} \\ &= \dot{V}_{\text{CHF,W}}'' \rho_{1} h_{\text{fg}} \left(\frac{A_{1}}{A_{\text{t}}}\right) \end{split} \tag{2}$$

where subscripts W and NW indicate wicking and nonwicking,  $m_{\rm CHF,W}$  is the liquid mass flow wicked under the apparent contact line at CHF,  $\dot{V}''_{\rm CHF,W}$  is the volumetric flux of liquid wicked into the surface at CHF, and  $A_{\rm t}$  is the total heated surface area. Nondimensionalizing eq 2 in the form of eq 1 yields

$$K_{\rm W} - K_{\rm NW} = \frac{A_{\rm l}}{A_{\rm t}} \left( \frac{\dot{V}_{\rm CHF,W}'' \rho_{\rm l}}{\rho_{\rm v}^{1/2} [\sigma g(\rho_{\rm l} - \rho_{\rm v})]^{1/4}} \right)$$
(3)

where the difference in K for wicking and nonwicking surfaces is proportional to the wetted area fraction as well as the wicked volume flux at CHF. The wetted area fraction has been observed to decline monotonically with increasing heat flux and drastically decreases as CHF is reached.<sup>43–46</sup> The minimum stable wetted area fraction at CHF has been measured to be anywhere from 50 to 90%, including recent work by Jung et al. using a novel infrared thermometry technique to measure the local wetting state and heat flux during the transition through CHF for FC-72.  $^{44}$ 

Equation 3 suggests that surfaces capable of wicking liquid at high rates will delay the unstable drop in wetted fraction associated with CHF. While measuring the wicked volume flux across a surface during an actual CHF event is extremely difficult, Ahn et al. reported a novel method of characterizing the rate of liquid flow drawn into a surface because of capillarity. Using a modified version of this approach, the wicked volume flux of each of the surfaces has been measured here. Figure 4a shows selected frames from high-speed imaging

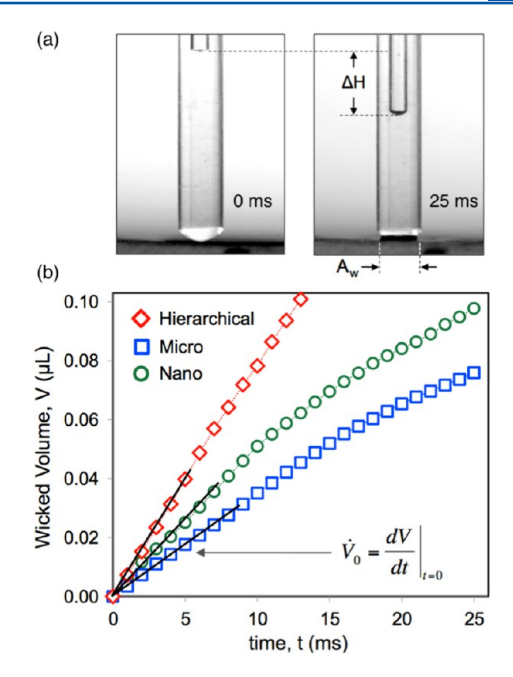


**Figure 4.** Experimental measurement of wickability. (a) High-speed imaging of water being drawn from a 500  $\mu$ m i.d. capillary tube after a structured surface is raised to contact a pendant droplet, resulting in wicking across the surface. (b) Experimental results of wicked volume as a function of time (for three select surfaces), calculated by tracking the displacement of the water level in the tube, showing the initial (maximum) volumetric flow rate.

where a structured surface is slowly raised to contact a pendant water droplet attached to a small-diameter capillary tube. As the surface makes contact with the droplet, liquid is wicked into the structures and the volumetric flow rate is measured by monitoring the liquid level in the tube. The maximum wicked volume flux is calculated as

$$\dot{V}_0'' = \frac{1}{A_W} \left(\frac{\mathrm{d}V}{\mathrm{d}t}\right)_{t=0} \tag{4}$$

where  $(dV/dt)_{t=0}$  is the initial (maximum) volume flow rate and  $A_{\rm W}$  is the apparent wetted area of the surface. As such,  $\dot{V}_0''$  is a measurable phenomenological parameter that characterizes the inherent wickability of a structured surface. This is analogous to characterizing wettability using the contact angle. Using this approach, the wicked volume flux captures the effects of micro/ nanostructure size, shape, morphology, permeability, intrinsic contact angle, and porosity all into one phenomenological parameter. This technique yields a direct measurement of the actual mass flow rate as opposed to the speed of a wicking front and therefore does not rely on assumptions regarding the permeability or geometry of the structures. This fact allows for a direct (and accurate) correlation with CHF via the additional latent heat associated with the wicked liquid mass flow. The structured surfaces fabricated in this work show no measurable contact angle (superhydrophilic), and the nonstructured hydrophilic surfaces show no measurable wicked volume flux. When the pendant droplet contacts a nonstructured sample, it deforms to wet the surface at its equilibrium contact angle. This deformation produces a negligible change in the volume of the pendant droplet as it bridges the gap between the tube and surface and results in no visible drop in the liquid level of the capillary tube. Complete details of the wicked volume flux measurement can be found in the Supporting Information.

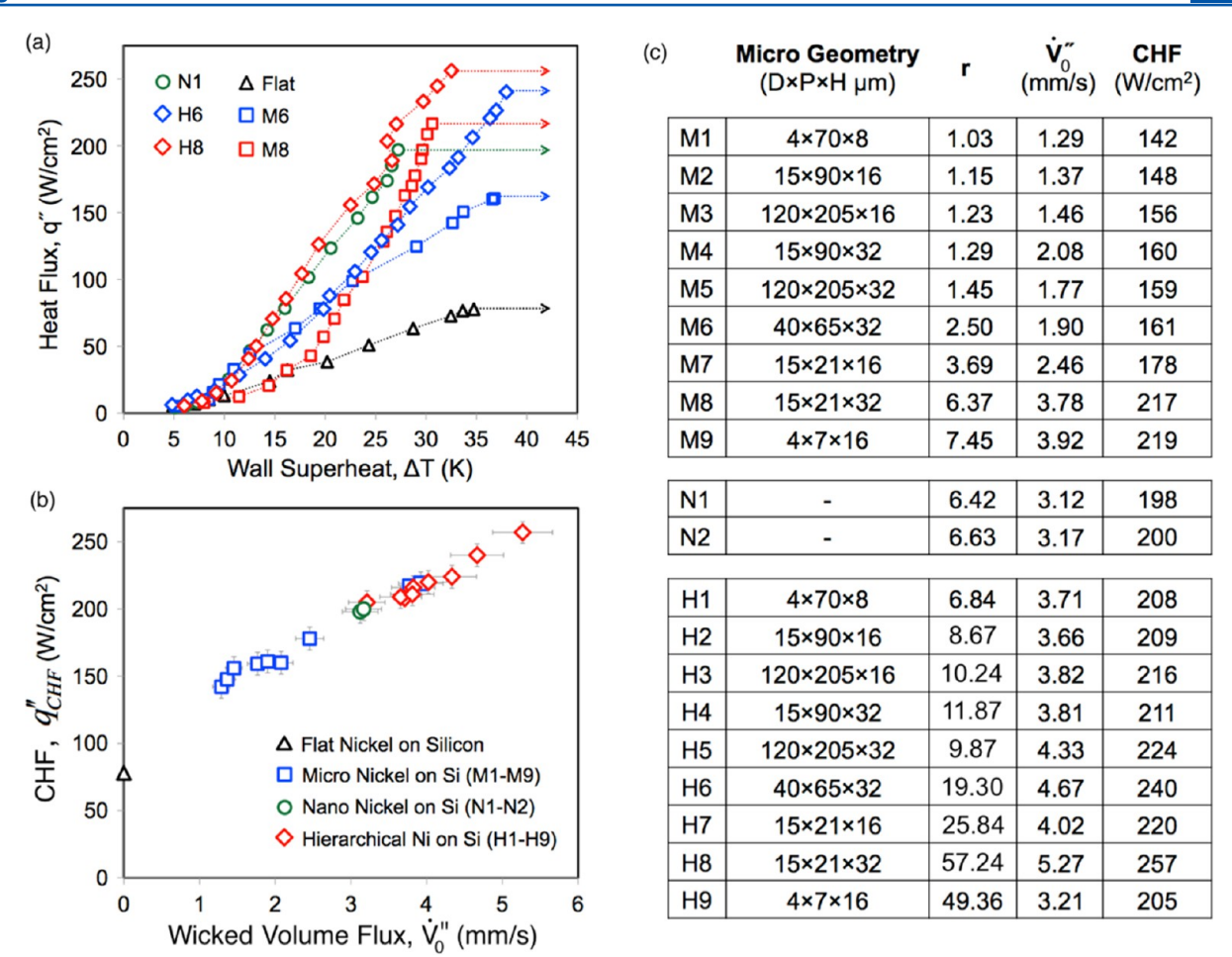


**Figure 5.** Experimental characterization of the CHF and wickability of structured silicon surfaces. (a) Boiling curves for six selected samples, where CHF is signified with an arrow. (b) Experimental results of CHF plotted against the wicked volume flux for all 20 silicon surfaces, showing a linear trend. (c) Details of the 20 micro, nano, and hierarchical silicon surfaces including the sample name, microstructure geometry (diameter × pitch × height), roughness factor, r, wicked volume flux,  $\dot{V}_0''$ , and CHF. See the Supporting Information for details on the measurements and their associated uncertainties.

The actual wicked volume flux experienced at CHF is a complicated function of the flow field including highly dynamic variations in the wetted area fraction, contact line speed, and contact line density during nucleate boiling. <sup>44</sup> It is assumed here, however, to scale linearly with the measured wicked volume flux,  $\dot{V}_{\text{CHF,W}}^{n} \propto \dot{V}_{0}^{n}$ , which is characterized using a quasistatic wetting state as shown in Figure 4. Equation 3 can therefore be rewritten as

$$K_{\rm W} - K_{\rm NW} \propto \left( \frac{\dot{V}_0'' \rho_1}{\rho_{\rm v}^{1/2} [\sigma g(\rho_1 - \rho_{\rm v})]^{1/4}} \right)$$
 (5)

where the proportionality is used because of the unknown wetted area fraction at CHF as well as the unknown proportionality between the actual wicked volume flux at CHF,  $\dot{V}''_{\text{CHF,W}}$ , and the measured wicked volume flux,  $\dot{V}''_{\text{O}}$ . This results in nondimensional CHF for a wicking surface,  $K_{\text{W}}$ , given by

$$K_{\rm W} = K_{\rm NW} + CWi \tag{6}$$

where  $K_{\rm NW}$  is the nondimensional CHF for the corresponding nonwicking surface, C is an unknown constant of proportionality, and Wi is defined here as the dimensionless wicking number given by

$$Wi \equiv \frac{\dot{V}_0'' \rho_1}{\rho_{\rm v}^{1/2} [\sigma g(\rho_1 - \rho_{\rm v})]^{1/4}}$$
 (7)

Wi is the nondimensional form of the wicked volume flux and represents the ratio of the liquid mass flux wicked into the surface structures relative to the critical mass flux of vapor leaving the surface as calculated using classical hydrodynamic instability analysis. <sup>42</sup> While previous models and results suggest a value of  $K_{\rm NW}$  of between 0.12 and 0.18 (Supporting Information), the unknown proportionality constant C and  $K_{\rm NW}$  have been empirically derived in the current work by measuring both the wickability and CHF of the structured surfaces fabricated here.

# MATERIALS AND METHODS

**Biotemplated Nanostructures.** Aluminum, copper, stainless steel, and gold-coated silicon were cut into a 1 cm  $\times$  1 cm sample, cleaned using acetone, IPA, and DI water, and immersed in 0.01–0.2 mg/mL virus solutions diluted in sodium phosphate buffer (pH 7.0). The TMV assembles onto the surfaces in a near vertical orientation during a 12–48 h time period. The TMV concentration and incubation time were varied to fabricate nanostructures on different surfaces with different densities. Following self-assembly of TMV, the samples are switched to a 1:15 mixture of 10 mM sodium(II) tetrachloropalladate (Na<sub>2</sub>PdCl<sub>4</sub>) and 0.1 M sodium phosphate buffer

for 2 to 3 h, where palladium nanoclusters form on the TMV. This Pd then acts as a catalyst for the electroless deposition of a  $\sim$ 40-nm-thick uniform nickel shell in a plating solution of nickel chloride hexahydrate (NiCl<sub>2</sub>·6H<sub>2</sub>O), glycine, sodium tetraborate (Na<sub>2</sub>B<sub>4</sub>O<sub>7</sub>), and dimethylamine borane (DMAB) for 4–8 min.

Microfabrication and Hierarchical Surfaces. Microstructured surfaces were fabricated from silicon substrates using traditional photolithography and deep reactive ion (DRIE) etching of a 4 in. wafer patterned using a positive photoresist (AZ 1512). The wafers were etched to the desired depths using an STS etcher and cleaned with oxygen plasma to remove the polymer passivation layer, followed by successive cleaning with acetone, IPA, and DI water. Then 35 nm of gold was sputtered on the microstructured wafer, and the wafers were diced into 1 cm  $\times$  1 cm samples. The hierarchical surfaces then underwent the TMV biotemplating process explained above to conformally coat the microstructures with nickel nanostructures. The microstructured samples went through an identical process, not including the TMV assembly step, resulting in a thin nickel coating directly over the silicon microposts.

**CuO Nanostructures.** Copper oxide nanostructures were fabricated on 1 cm  $\times$  1 cm copper samples that were first sanded with 200 grit sandpaper; cleaned with acetone, IPA, and DI water; and stripped of native oxides in a 2 M hydrochloric acid bath. Five different CuO samples were fabricated using different chemical compositions, bath temperatures, and reaction times and then rinsed with DI water and dried with N<sub>2</sub>. The solution temperatures were continuously monitored using a T-type thermocouple and maintained within 2 °C of the reported value throughout growth. Complete details of the conditions are listed in Figure 7a—e, including the recipes reported by Chu et al. <sup>28</sup> (Figure 7a) and Love et al. <sup>47</sup> (Figure 7d).

# RESULTS AND DISCUSSION

To characterize the effects of wickability on CHF, the micro, nano, and hierarchically structured silicon surfaces shown in Figure 2 were tested during the nucleate pool boiling of water under atmospheric conditions. Figure 5a shows selected boiling curves for several of the designs where CHF is signified with a horizontal arrow. Details of the pool boiling setup, test procedures, and measurements as well as the complete data sets for each design can be found in the Supporting Information. Additionally, the Supporting Information contains comparisons against published results from other researchers for pool boiling on flat and structured surfaces, showing excellent agreement and thus validating the accuracy of the experimental method. Figure 5b shows CHF as a function of the experimentally measured wicked volume flux,  $\dot{V}_0''$ , for all 20 structured silicon samples as well as a single flat silicon sample. Figure 5c shows the complete legend for all of the tests including sample names, micropost array geometries, roughness factors, wickabilities, and CHF values. As can be seen from Figure 5b, a clear and distinct linear relationship between CHF and the wicked volume flux exists, as predicted from the closedform model. Further examination shows that no such relationship can be seen between CHF and the roughness factor. Section S5 of the Supporting Information provides a complete description of the measurement of the roughness factor as well as its correlation with CHF (Figure S9). While Chu's model shows general agreement for well-defined microposts and surfaces with low-to-moderate roughness factors (r < 10), it greatly overpredicts CHF for large roughness factors (r > 10), including many of the nanostructured and hierarchical surfaces reported here and in the open literature. 21,22,26,29

Using a hierarchical design, a maximum CHF of 257 W/cm<sup>2</sup> has been achieved at a wicked volume flux of over 5 mm/s. This represents the highest reported CHF for water on a silicon

substrate as well as the highest reported CHF for a superhydrophilic surface (contact angle  $\sim\!\!0^{\circ}$ ) on any substrate. This result is comparable to the work of Chu et al.  $^{28}$  using hierarchical surfaces to show a CHF of 250 W/cm². Additionally, it is seen that microstructured designs can also exhibit high wickability and CHF, with values of nearly 4 mm/s and 220 W/cm², respectively. The nanostructured surfaces provide a CHF of around 200 W/cm², consistent with prior results.  $^{24}$ 

**Effect of Substrate, Nanostructure Density, and Fouling.** Depending on variations in the substrate material as well as the micro/nanostructures themselves, wickability can vary from sample to sample, spatially across a surface as well as over time. This includes the effects of surface defects and variations in structure density as well as degradation due to fouling. To investigate these effects, various TMV-templated nanostructured surfaces have been fabricated and tested on nonsilicon substrates, as first demonstrated in prior work by the authors.<sup>24</sup> In that work, the TMV biotemplating technique was optimized for deposition onto aluminum, copper, and stainless steel. During the optimization process, a variety of nonideal surface coatings were created with lower-quality surface coverages. Figure 6a shows SEM images of the results of an

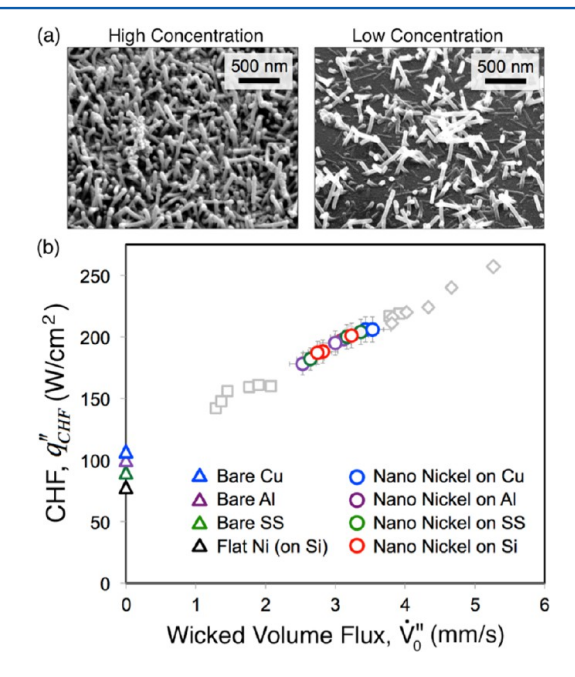


Figure 6. Effect of substrate material, TMV morphology, and fouling on wicking-enhanced CHF. (a) SEM images showing high-concentration and low-concentration TMV coatings. (b) CHF as a function of wicked volume flux for TMV nanostructures on multiple metallic substrates, showing variations in performance due to differences in morphology as well as fouling after repeated testing. The results are compared to the corresponding bare surfaces as well as the micro, nano, and hierarchal silicon surfaces (light-gray symbols).

optimized deposition, with a high concentration of nickel nanostructures, as compared to an unoptimized deposition with a low concentration. Additionally, Rahman et al. showed that a slight decrease in CHF ( $\sim$ 5%) is observed after repeated testing of the surfaces, including repeated CHF and burnout events. <sup>24</sup> This decrease was attributed to reversible fouling, and after being cleaned, the surfaces returned to their initial values.

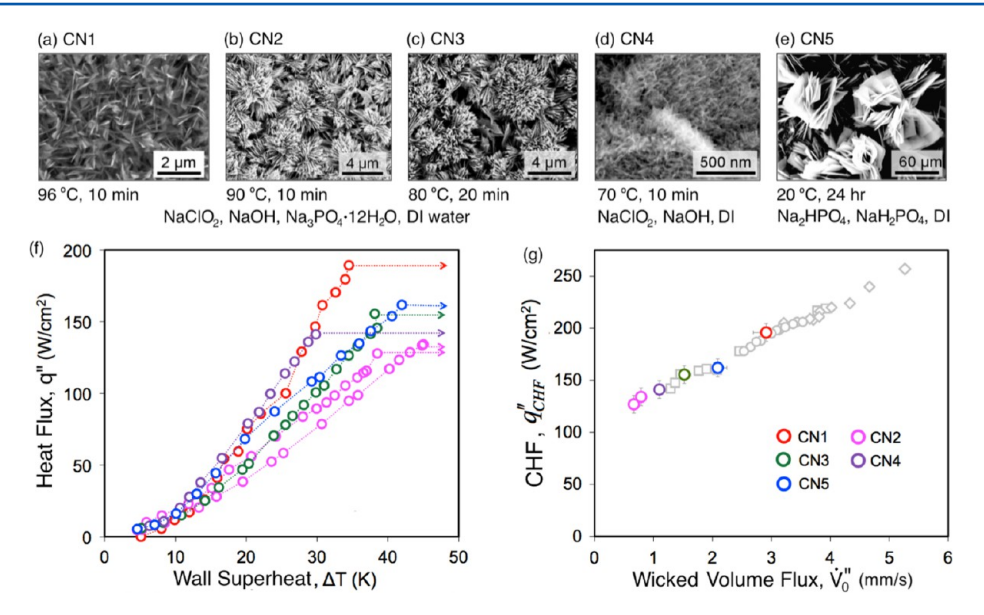


Figure 7. Copper oxide nanostructured coatings. (a-e) SEM images of five different CuO nanostructured coatings and the corresponding fabrication conditions, including solution temperature, time, and composition. (f) Boiling curves and (g) CHF as a function of wicked volume flux, showing consistency with TMV-structured micro, nano, and hierarchical coatings on silicon and metallic substrates (light-gray symbols).

The performance of TMV coatings with varying nanostructure densities, as well as those degraded by fouling, were measured to characterize the impact on both wickability and CHF. Figure 6b shows the CHF versus wickability data for silicon, aluminum, copper, and stainless steel surfaces with both high- and low-density coatings as well as samples degraded by fouling after repeated testing. As can be seen, the variation in TMV density and surface fouling leads to variations in the measured CHF. However, these variations are accompanied by corresponding variations in the measured wickability, with the data closely following the linear trend seen for micro, nano, and hierarchical silicon surfaces. This is strong evidence pointing to wickability as not only the key factor in CHF enhancement but also a convenient phenomenological parameter that is easily measured and accurately accounts for the complex effects of variations in morphology, surface defects, and degradation due to fouling.

Effect of Nanostructure Material and Morphology. To compare the results for TMV-structured surfaces with alternative materials and structures, a series of copper oxide nanostructured surfaces have also been fabricated and characterized. CuO nanostructures are ideal for this comparison because of the ability to easily tune their morphologies as well as the availability of existing pool boiling data.<sup>28°</sup> Figure 7a shows the five distinct CuO nanostructures fabricated and tested in this work, along with the chemical composition, bath temperature, and growth times used to create each. Surface CN1 (Figure 7a) was produced using the recipe reported by Chu et al., 28 while surfaces CN2 and CN3 use the same alkaline bath but vary the temperature and/or growth time. CN4 (Figure 7d) was produced using the method reported by Love et al., 47 and CN5 (Figure 7e) was produced by immersing a copper sample into a simple bath of phosphate buffer at room temperature. Figure 7f,g shows the resulting boiling curves and CHF as a function of wickability. Figure S5 in the Supporting Information shows nearly identical boiling curves for the CN1 sample and the results obtained by Chu et al., 28 verifying the accuracy and repeatability of both the fabrication and testing procedures. While it is difficult to quantify the variations in

surface morphology and roughness factor for the five CuO nanostructures shown in Figure 7a—e, the wickability of each sample is easily measured. Additionally, it can be seen that a small change in bath conditions between CN1 and CN2 (90 to 96  $^{\circ}$ C) leads to noticeable variations in CHF (56% increase). Nevertheless, Figure 7g shows that the enhancement of CHF is due to wickability and is consistent with the results from the nickel-coated TMV-structured surfaces.

**Effect of Wickability on CHF.** Figure 8a,b shows the entirety of the CHF data collected for all of the surfaces fabricated and tested in this work, including nonstructured hydrophilic and structured superhydrophilic surfaces, plotted against the surface wickability (Figure 8a) and surface wettability (Figure 8b). The nonstructured surfaces exhibit measurable contact angles and no measurable wickability, while the structured samples exhibit varying wickability but no measurable contact angle. For nonwicking surfaces, CHF is consistent with existing literature and established models from Zuber<sup>7</sup> and Kandlikar. <sup>16</sup> The CHF of structured superhydrophilic surfaces, however, cannot be predicted using traditional modeling approaches. This trend is commonly shown in the open literature, including the large spread in data at a contact angle of 0°.

Fitting the data shown in Figure 8a with the linear relationship predicted by eq 6 yields a value of  $K_{\rm NW}=K_{\rm Zuber}=0.131$ . This is consistent with numerous experimental results validating Zuber's limit for flat surfaces not capable of capillary wicking. Interestingly, this fit also yields a value of  $C=K_{\rm Zuber}=0.131$ , suggesting a nondimensional correlation for CHF on structured superhydrophilic surfaces of the form

$$K_{\rm W} = K_{\rm Zuber}(1 + Wi) \tag{8}$$

where the dimensionless wicking number, *Wi*, is given by eq 7. Rearranging terms, this results in a CHF enhancement factor relative to Zuber's limit of

$$\frac{q_{\text{CHF,W}}^{"}}{q_{\text{CHF,Zuber}}^{"}} = 1 + Wi \tag{9}$$

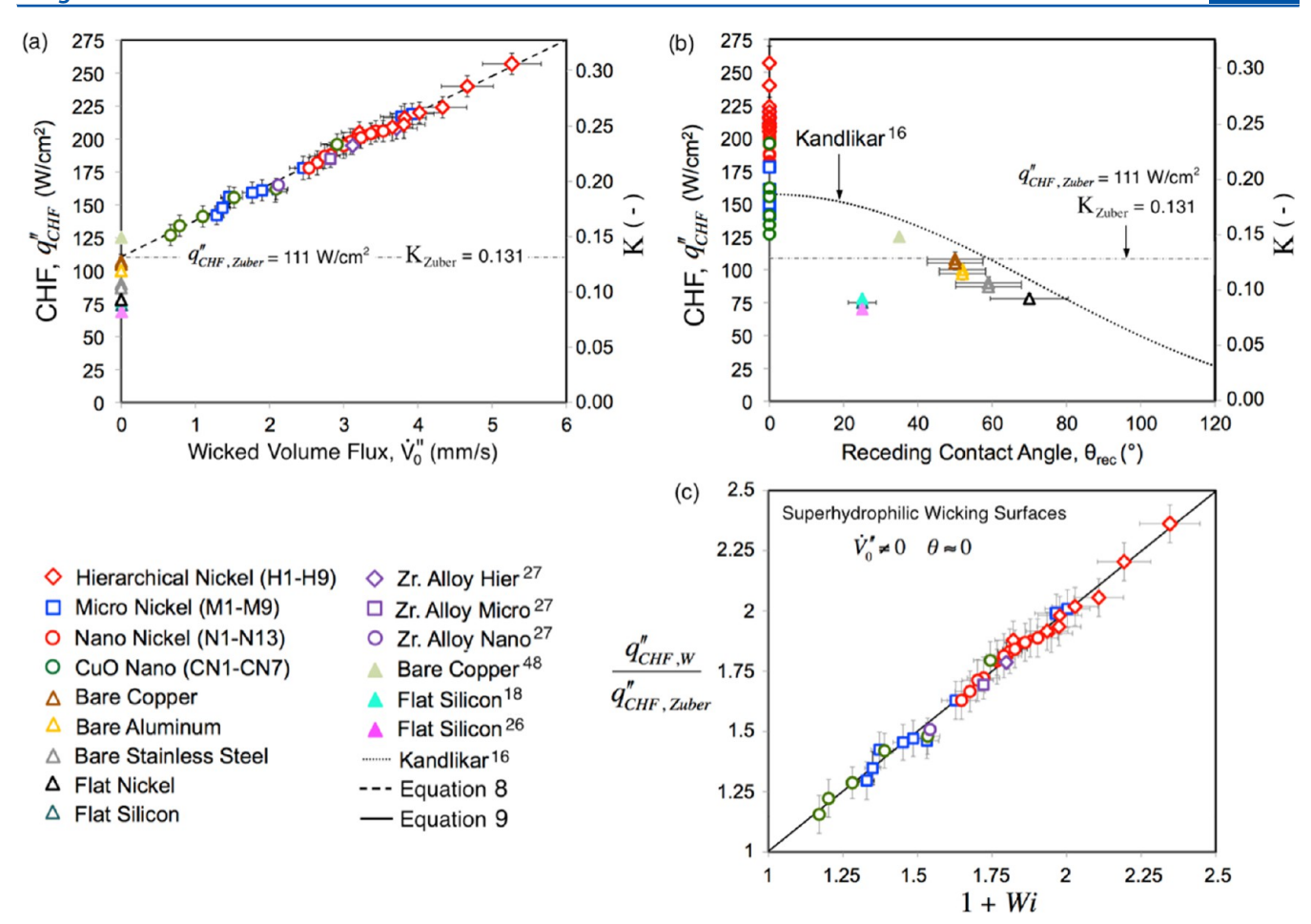


**Figure 8.** Effect of wickability on CHF. Experimentally measured CHF as a function of (a) wicked volume flux and (b) receding contact angle for over 40 individual surfaces, showing the importance of wickability for structured superhydrophilic surfaces. The data includes variations in scale (micro, nano, hierarchical), morphology, fouling, structure material, and substrate material as well as data from other researchers. (c) CHF enhancement as a function of wicking number, *Wi*, for superhydrophilic surfaces showing excellent agreement with the developed correlation given by eq 9 as well as data from other researchers. <sup>18,26,27,48</sup>

Figure 8c shows the experimental data for each of the superhydrophilic surfaces fabricated here, matching the CHF enhancement factor given by eq 9 to well within the measured experimental uncertainty (<10%). The resulting enhancement factor given by eq 9 is consistent in nature with the analytically derived model for CHF enhancement due to capillary wicking reported by Guan et al.,<sup>41</sup> including the definition of a nondimensional parameter capturing the surfaces' ability to wick. That work used the speed of a hemiwicking front of hexane and FC-72 as the relevant measure of wickability (as compared to the wicked volume flux used here), thus precluding a direct comparison of the experimental results. In addition to the 40 individual samples fabricated and tested in this work, Figure 8 includes results from Ahn et al. using micro, nano, and hierarchically structured zirconium alloy. This data was extracted from the reported CHF, adsorbed volume measurements, and optical images of capillary wicking experiments. These results show that wickability (quantified here by the wicked volume flux and dimensionless wicking number, Wi) is the critical parameter dictating CHF on structured superhydrophilic surfaces. A definitive and consistent linear relationship for CHF with respect to wickability is seen, as predicted by the simple analytic model. These results are independent of variations in the structure length scale (micro, nano, and hierarchical), substrate material (silicon, aluminum,

stainless steel, copper, and zirconium), nanostructure density, roughness factor, degradation due to fouling, and surface structure material and morphology (etched silicon micropost arrays, virus-templated nickel nanostructures, copper oxide nanostructures, and anodized zirconium).

#### CONCLUSIONS

Biological templates have been used here to demonstrate that wickability is the single key factor in dictating critical heat flux on structured superhydrophilic surfaces with negligible contact angles. The flexibility and simplicity of biotemplated nanofabrication using the Tobacco mosaic virus has been leveraged to create a wide range of structured surfaces with varying scales, morphologies, roughness factors, and wickabilities. By quantifying the wickability of a surface via the wicked volume flux (a phenomenological parameter analogous to the contact angle), the role of wickability in CHF enhancement has been clearly demonstrated using data from over three dozen individual samples. These results were shown to be repeatable and independent of the substrate material or finish; observed degradation due to fouling; the material, morphology, and intrinsic contact angle of the surface structures; and the scale of the surface structure (micro, nano, hierarchical). This has yielded an experimentally validated nondimenaional correlation for CHF enhancement, including the definition of the

dimensionless wicking number, *Wi*. Additionally, virus-structured hierarchical surfaces have been shown to enhance CHF up to 257 W/cm² for water under atmospheric conditions, the highest reported value to date for a superhydrophilic coating. While the role of wickability in CHF enhancement has often been cited anecdotally, this work provides a quantitative and definitive measure of the phenomena and provides both insights into the mechanisms of CHF as well as a framework for designing and optimizing coatings for further enhancement.

#### ASSOCIATED CONTENT

# **S** Supporting Information

The *Tobacco mosaic virus* and biotemplated nanofabrication, CHF modeling, wickability characterization, pool boiling characterization, roughness factor, and uncertainty analysis. This material is available free of charge via the Internet at http://pubs.acs.org.

# AUTHOR INFORMATION

# **Corresponding Author**

\*E-mail: mccarthy@coe.drexel.edu.

#### **Notes**

The authors declare no competing financial interest.

#### ACKNOWLEDGMENTS

Support for this work was provided by the National Science Foundation (grant no. CBET-1264958).

#### REFERENCES

- (1) Kim, J. Review of nucleate pool boiling bubble heat transfer mechanisms. *Int. J. Multiphase Flow* **2009**, 35, 1067–1076.
- (2) Lu, Y.-W.; Kandlikar, S. G. Nanoscale Surface Modification Techniques for Pool Boiling Enhancement—A Critical Review and Future Directions. *Heat Transfer Eng.* **2011**, 32, 827–842.
- (3) Bergles, A. E. What is the real mechanism of CHF in pool boiling? Proceedings of the Engineering Foundation Conference on Pool and External Flow Boiling; ASME: New York, 1992; pp 165–170.
- (4) Kutateladze, S. S. On the Transition to Film Boiling under Natural Convection. *Kotloturbostroenie* **1948**, 3, 10–12.
- (5) Kutateladze, S. S. A Hydrodynamic Theory of Changes in a Boiling Process Under Free Convection. *Izvestia Akademia Nauk*, S.S.S.R., Otdelenie Tekhnicheski Nauk 1951, 4, 529.
- (6) Lienhard, J. H.; Dhir, V. K. Hydrodynamic Prediction of Peak Pool-boiling Heat Fluxes from Finite Bodies. *J. Heat Transfer* **1973**, *95*, 152–158.
- (7) Zuber, N. Hydrodynamic Aspects of Boiling Heat Transfer. University of California: Los Angeles, Cailfornia, 1959.
- (8) Rohsenow, W. M., Griffith, P. Correlation of maximum heat flux data for boiling of saturated liquids. *Chem. Eng. Prog.* **1955**, 52.
- (9) Haramura, Y.; Katto, Y. A new hydrodynamic model of critical heat flux, applicable widely to both pool and forced convection boiling on submerged bodies in saturated liquids. *Int. J. Heat Mass Transfer* **1983**, *26*, 389–399.
- (10) Rajvanshi, A. K.; Saini, J. S.; Prakash, R. Investigation of Macrolayer Thickness in Nucleate Pool Boiling at High Heat-Flux. *Int. J. Heat Mass Transfer* **1992**, *35*, 343–350.
- (11) Sakashita, H.; Ono, A. Boiling behaviors and critical heat flux on a horizontal plate in saturated pool boiling of water at high pressures. *Int. J. Heat Mass Transfer* **2009**, *52*, 744–750.
- (12) Guan, C.-K.; Klausner, J. F.; Mei, R. A new mechanistic model for pool boiling CHF on horizontal surfaces. *Int. J. Heat Mass Transfer* **2011**, *54*, 3960–3969.
- (13) Dhir, V. K.; Liaw, S. P. Framework for a Unified Model for Nucleate and Transition Pool Boiling. *J. Heat Transfer* **1989**, 111, 739–746.

(14) Kirichenko, Y. A.; Chernyakov, P. S. Determination of the first critical thermal flux on flat heaters. *J. Eng. Phys.* **1971**, *20*, 699–703.

- (15) Ramilison, J. M.; Sadasivan, P.; Lienhard, J. H. Surface Factors Influencing Burnout on Flat Heaters. *J. Heat Transfer* **1992**, *114*, 287–290.
- (16) Kandlikar, S. G. A Theoretical Model to Predict Pool Boiling CHF Incorporating Effects of Contact Angle and Orientation. *J. Heat Transfer* **2001**, 123, 1071–1079.
- (17) Bon, B. K.; J, F.; McKenna, E. The Hoodoo: A New Surface Structure for Enhanced Boiling Heat Transfer. *J. Thermal Sci. Eng. Appl.* **2013**, *5*, 011003.
- (18) Chu, K.-H.; Enright, R.; Wang, E. N. Structured surfaces for enhanced pool boiling heat transfer. *Appl. Phys. Lett.* **2012**, *100*, 241603.
- (19) O'Hanley, H.; Coyle, C.; Buongiorno, J.; McKrell, T.; Hu, L.-W.; Rubner, M.; Cohen, R. Separate effects of surface roughness, wettability, and porosity on the boiling critical heat flux. *Appl. Phys. Lett.* **2013**, *103*, 024102.
- (20) Zou, A.; Maroo, S. C. Critical height of micro/nano structures for pool boiling heat transfer enhancement. *Appl. Phys. Lett.* **2013**, *103*, 221602.
- (21) Chen, R.; Lu, M.-C.; Srinivasan, V.; Wang, Z.; Cho, H. H.; Majumdar, A. Nanowires for Enhanced Boiling Heat Transfer. *Nano Lett.* **2009**, *9*, 548–553.
- (22) Li, C.; Wang, Z.; Wang, P. I.; Peles, Y.; Koratkar, N.; Peterson, G. P. Nanostructured copper interfaces for enhanced boiling. *Small* **2008**, *4*, 1084–1088.
- (23) Lu, M.-C.; Chen, R.; Srinivasan, V.; Carey, V. P.; Majumdar, A. Critical heat flux of pool boiling on Si nanowire array-coated surfaces. *Int. J. Heat Mass Transfer* **2011**, *54*, 5359–5367.
- (24) Rahman, M. M.; Ölçeroğlu, E.; McCarthy, M. Scalable Nanomanufacturing of Virus-Templated Coatings for Enhanced Boiling. *Adv. Mater. Interfaces* **2014**, *1*, 1300107.
- (25) Sathyamurthi, V.; Ahn, H. S.; Banerjee, D.; Lau, S. C. Subcooled Pool Boiling Experiments on Horizontal Heaters Coated With Carbon Nanotubes. *J. Heat Transfer* **2009**, *131*, 071501.
- (26) Yao, Z.; Lu, Y. W.; Kandlikar, S. G. Effects of nanowire height on pool boiling performance of water on silicon chips. *Int. J. Therm. Sci.* **2011**, *50*, 2084–2090.
- (27) Ahn, H. S.; Park, G.; Kim, J. M.; Kim, J.; Kim, M. H. The effect of water absorption on critical heat flux enhancement during pool boiling. *Exp. Therm Fluid Sci.* **2012**, 42, 187–195.
- (28) Chu, K.-H.; Soo Joung, Y.; Enright, R.; Buie, C. R.; Wang, E. N. Hierarchically structured surfaces for boiling critical heat flux enhancement. *Appl. Phys. Lett.* **2013**, *102*, 151602.
- (29) Kim, S.; Kim, H. D.; Kim, H.; Ahn, H. S.; Jo, H.; Kim, J.; Kim, M. H. Effects of nano-fluid and surfaces with nano structure on the increase of CHF. *Exp. Therm Fluid Sci.* **2010**, *34*, 487–495.
- (30) Yao, Z.; Lu, Y.-W.; Kandlikar, S. G. Pool Boiling Heat Transfer Enhancement Through Nanostructures on Silicon Microchannels. *J. Nanotechnol. Eng. Med.* **2012**, *3*, 031002.
- (31) Betz, A. R.; Jenkins, J.; Kim, C. J.; Attinger, D. Boiling heat transfer on superhydrophilic, superhydrophobic, and superbiphilic surfaces. *Int. J. Heat Mass Transfer* **2013**, *57*, 733–741.
- (32) Betz, A. R.; Xu, J.; Qiu, H.; Attinger, D. Do surfaces with mixed hydrophilic and hydrophobic areas enhance pool boiling? *Appl. Phys. Lett.* **2010**, *97*, 141909.
- (33) Kandlikar, S. G. Controlling bubble motion over heated surface through evaporation momentum force to enhance pool boiling heat transfer. *Appl. Phys. Lett.* **2013**, *102*, 051611.
- (34) Knez, M.; Sumser, M. P.; Bittner, A. M.; Wege, C.; Jeske, H.; Hoffmann, D. M. P.; Kuhnke, K.; Kern, K. Binding the tobacco mosaic virus to inorganic surfaces. *Langmuir* **2004**, *20*, 441–447.
- (35) Fan, X.; Pomerantseva, E.; Gnerlich, M.; Brown, A.; Gerasopoulos, K.; McCarthy, M.; Culver, J.; Ghodssi, R. Tobacco Mosaic Virus: An Integratable Biotemplate for Micro/Nano Systems. *J. Vac. Sci. Technol.* **2013**, *31*, 050815.
- (36) Gerasopoulos, K.; Pomerantseva, E.; McCarthy, M.; Brown, A.; Wang, C.; Culver, J.; Ghodssi, R. Hierarchical Three-Dimensional

Microbattery Electrodes Combining Bottom-Up Self-Assembly and Top-Down Micromachining. ACS Nano 2012, 6, 6422–6432.

- (37) McCarthy, M.; Gerasopoulos, K.; Enright, R.; Culver, J. N.; Ghodssi, R.; Wang, E. N. Biotemplated hierarchical surfaces and the role of dual length scales on the repellency of impacting droplets. *Appl. Phys. Lett.* **2012**, *100*, 263701.
- (38) Gerasopoulos, K.; McCarthy, M.; Banerjee, P.; Fan, X.; Culver, J. N.; Ghodssi, R. Biofabrication Methods for The Patterned Assembly and Synthesis of Viral Nanotemplates. *Nanotechnology* **2010**, *21*, 055304.
- (39) Gerasopoulos, K.; McCarthy; Royston, E.; Culver, J. N.; Ghodssi, R. Nanostructured Nickel Electrodes using the Tobacco Mosaic Virus for Microbattery Applications. *J. Micromech. Microeng.* **2008**, *18*, 104003.
- (40) Ölçeroğlu, E.; Hsieh, C. Y.; Rahman, M. M.; Lau, K. K. S.; McCarthy, M. Full-Field Dynamic Characterization of Superhydrophobic Condensation on Biotemplated Nanostructured Surfaces. *Langmuir* **2014**, *30*, 7556–7566.
- (41) Guan, C. K.; Bon, B.; Klausner, J.; Mei, R. W. Comparison of CHF Enhancement on Microstructured Surfaces With a Predictive Model. *Heat Transfer Eng.* **2014**, *35*, 452–460.
- (42) Carey, V. P. Liquid-Vapor Phase-Change Phenomena; Taylor and Francis: New York, 2008.
- (43) Chu, I. C.; No, H. C.; Song, C. H. Visualization of boiling structure and critical heat flux phenomenon for a narrow heating surface in a horizontal pool of saturated water. *Int. J. Heat Mass Transfer* **2013**, *62*, 142–152.
- (44) Jung, J.; Kim, S. J.; Kim, J. Observations of the Critical Heat Flux Process During Pool Boiling of FC-72. *J. Heat Transfer* **2014**, *136*, 041501.
- (45) Kim, H.; Park, Y.; Buongiorno, J. Measurement of Wetted Area Fraction in Subcooled Pool Boiling of Water Using Infrared Thermometry. *Nucl. Eng. Des.* **2013**, 264, 103–110.
- (46) Theofanous, T. G.; Dinh, T. N.; Tu, J. P.; Dinh, A. T. The boiling crisis phenomenon Part II: dryout dynamics and burnout. *Exp. Therm Fluid Sci.* **2002**, *26*, 793–810.
- (47) Love, B. J.; Packman, P. F. Effects of Surface Modifications on the Peel Strength of Copper-Based Polymer-Metal Interfaces with Characteristic Morphologies. *J. Adhesion* **1993**, *40*, 139–150.
- (48) Cooke, D.; Kandlikar, S. G. Pool Boiling Heat Transfer and Bubble Dynamics Over Plain and Enhanced Microchannels. *J. Heat Transfer* **2011**, 133, 052902.